1	Indirect assimilation of radar reflectivity data with an adaptive
2	hydrometer retrieval scheme for the short-term severe weather
3	forecasts
4	
5	Lixin Song ¹ , Feifei Shen ^{1,2,3,4*} , Zhixin He ⁵ , Lu Yang ¹ , Dongmei Xu ¹ , Aiqing Shu ¹ , and Jiajun
6	Chen ¹
7	
8	¹ Key Laboratory of Meteorological Disaster, Ministry of Education (KLME) /Joint
9	International Research Laboratory of Climate and Environment Change (ILCEC) /Collaborative
10	Innovation Center on Forecast and Evaluation of Meteorological Disasters (CIC-FEMD), Nanjing
11	University of Information Science & Technology, Nanjing 210044, China
12	
13	² Key Laboratory of Urban Meteorology, China Meteorological
14	Administration, Beijing 100089, China China Meteorological Administration Tornado Key
15	Laboratory
16	
17	³ China Meteorological Administration Tornado Key Laboratory China Meteorological
18	Administration Radar Meteorology Key Laboratory, Nanjing 210000, China
19	
20	
21	⁴ China Meteorological Administration Radar Meteorology Key Laboratory, Nanjing 210000,
22	China Shanghai Typhoon Institute, China Meteorological Administration, Shanghai 200030, China
23	
24	⁵ Anhui Meteorological Observatory, Hefei 230000, China
25	
26	June October 20242025
27	
28	*Corresponding author address:
29	Feifei Shen
30	Nanjing University of Information Science & Technology
31	ffshen@nuist.edu.cn

32 Abstract

33

34

35

36

37

38

39 40

41

42

43

44 45

46

47

48

49

50

51 52

53

54

55

56

57 58

59

60

Different hydrometeor retrieval schemes are explored based on the Weather Research and Forecasting (WRF) model in the indirect assimilation of radar reflectivity for two real cases occurred during June 2020 and August 2018. When retrieving hydrometeors from radar reflectivity, there are two commonly used hydrometeor classification methods: "temperature-based" and "background hydrometer-dependent" schemes. The hydrometeor proportions are usually empirically assigned in the "temperature-based" method within different background temperature intervals. Whereas, in the "background hydrometer-dependent" scheme, each type of the hydrometeor is derived based on the portions estimated from the background field for different radar reflectivity ranges. In this study, a blending scheme is designed to combine "temperature-based" and "background hydrometer-dependent" methods adaptively to avoid errors caused by fixed relationships and reduce uncertainties introduced by the background field itself. Three experiments, EXP_temp, EXP_bg, and EXP_temp-bg are conducted using the "temperature-based" method, "background hydrometer-dependent" scheme, and blending scheme, respectively. It is found that, adding the "background hydrometer-dependent" schemethe blending scheme facilitates the generation of accurate hydrometeor species which will enhance the effectiveness of radar data assimilation. EXP_temp bg is capable of analyzing radar reflectivity structures more accurately compared to both EXP temp and EXP bg. Besides, due to the adaptive combination of "temperature-based" and "background hydrometer-dependent" schemes, the EXP temp-bg experiment yields the improved thermodynamic and dynamic structures, which contributes to predict radar reflectivity and the radar reflectivity structures and precipitation intensity more accurately.

Key words: Numerical weather prediction, Radar data assimilation, Hydrometeor retrieval.

1. Introduction

The initial condition is a crucial factor in enhancing the accuracy of numerical weather prediction (NWP, Navon, 2009; Kain et al., 2010; Lopez, 2011; Xu et al., 2021). Compared to conventional

observations, doppler radar observations have extremely high temporal and spatial resolution, as

带格式的: 缩进: 首行缩进: 0字符

well as containing precipitating hydrometeor information (Zhao et al., 2012; Li et al., 2013; Kong et al., 2020). Therefore, radar is one of the key platforms for obtaining proper initial conditions to successfully predict convective storms (Lilly, 1990; Dawson et al., 2015; Gustafsson et al., 2018; Shen et al., 2020a; Xu et al., 2022; Chen et al., 2023). A number of efforts have been devoted to assimilating radar data into mesoscale numerical models (Lindskog et al., 2004; Dowell et al., 2011; Sun et al., 2014; Bick et al., 2016; Tong et al., 2020; Shen et al., 2016, 2019, 2022; Wan et al., 2024). Radar observations have two fundamental variables: radar radial velocity (Vr) and radar reflectivity (Z). Assimilating radar radial velocity is conducive to improving the dynamical structure of the initial field. Numerous scholars are dedicated to researching radar radial velocity assimilation (Gao et al., 2004; Simonin et al., 2014; Li et al., 2016; Shen et al., 2020b). Based on the threedimensional variational (3DVar) system of the fifth generation Pennsylvania State University-NCAR Mesoscale Model (MM5), Xiao et al. (2005) developed a radar radial velocity observation operator, and investigated the impact of assimilating radar radial velocity on precipitation forecasts. Besides, Wang et al. (2013b) employed the four-dimensional variational (4DVar) system to assimilate radar radial velocity and reflectivity into the model for enhancing forecasting accuracy. In contrast, assimilating radar reflectivity is more challenging than assimilating the radial wind, on account of its highly nonlinear observation operator and close relationship with complex microphysics (Borderies et al., 2019; Xu et al., 2019). Currently, there are two main methods for assimilating radar reflectivity: direct assimilation and indirect assimilation. Xiao et al. (2007) proposed a direct assimilation scheme for radar reflectivity based on the 3DVar system of MM5. The water content was classified according to phases using warm rain microphysical processes. However, due to the absence of ice-phase particles, the scheme demonstrates limited effectiveness in deep moist convection cases that are dominated by cold-cloud processes. However, due to the absence of ice phase particles, the scheme showed limited effectiveness in deep moist convection cases dominated by cold cloud processes. the positive impact is not promising in cases of deep moist convections generated through cold-cloud processes. To assimilate radar reflectivity into numerical weather prediction (NWP) models more effectively, Gao and Stensrud (2012) proposed a hydrometeor classification method based on the 3DVar system in the direct assimilation of radar reflectivity. The results demonstrated that this classification method benefits to accelerate the

61

62

63

64 65

66 67

68

69

70

71

72

73

74

75

76

77

78

79

80

81

82

83

84

85

86

87

88 89 convergence speed of the analysis and reduce errors in the analysis. Compared to variational data assimilation methods, Ensemble Kalman Filter (EnKF; Evensen, 1994) is a better choice for assimilating radar reflectivity directly, since EnKF does not require consideration of the tangent or adjoint model of the observation operator (Liu et al., 2019). Based on the EnKF method, Tong and Xue (2005) assimilated the simulated radar observations from a supercell storm. The results indicated that directly assimilating radar reflectivity data has a positive impact on both analyses and forecasts. Although the forward operator of reflectivity tends to be easily implemented in EnKF, its computational cost is too high to be widely applied in the scientific research and operational forecasting (Kong et al., 2018). To avoid the issue of high nonlinearity in radar reflectivity observation operators, the indirect assimilation method is often used in the NWP. Based on the Advance Regional Prediction System (ARPS), Hu et al. (2006) investigated the impact of cloud analysis using radar reflectivity on forecasting tornado storms. They found that cloud analysis helps to adjust the temperature, humidity fields, and hydrometeors within the clouds, thereby improving tornado predictions. Also, Schenkman et al. (2011) found that cloud analysis technology is able to adjust cloud variables to better suit the dynamic and thermal fields. However, cloud analysis schemes rely largely on uncertain empirical relationships, thus usually hardly suppressing the generation of spurious echoes. Using the 4DVar system, Sun and Crook (1997) proposed to assimilate rainwater mixing ratios retrieved from reflectivity instead of directly assimilating reflectivity, which seems to produce better analysis results. Based on the 3DVar system of WRF, Wang et al. (2013a) further demonstrated that assimilation of rainwater and estimated water vapor obtained from radar reflectivity reduces the linearization error of the radar reflectivity observation operator, thus improving precipitation forecasts. However, both indirect assimilation methods under the two variational frameworks are employed in the warm-rain scheme, which restricts their applications above troposphere or in the coexistence of liquid and ice particles. Shen et al. (2021) added hydrometeor control variables included ice-phase particles when indirectly assimilating radar reflectivity observations of Hurricane IKE, which enables track and intensity forecasts of the hurricane to be greatly improved. For the indirect assimilation of radar reflectivity, one of the challenges is how to correctly classify

90

91

92

93

94

95

96

97

98

99

100101

102

103

104

105

106

107

108

109

110

111

112

113

114

115

116

117

118

hydrometeors in observations. There are currently two methods to distinguish hydrometeor types.

One is to classify hydrometeor types according to background temperature (hereafter called temperature-based) developed by Gao and Stensrud (2012), with fixed parameters and empirical relations. Another is the "background hydrometer-dependent" hydrometeor retrieval scheme (Chen et al., 2020, 2021). The "background hydrometer-dependent" method calculates hydrometeor weights in various thresholds from the model background field to better allocate radar reflectivity observation information. This approach avoids empirical thresholds and weighting coefficients given in the "temperature-based" method, and benefits to improve the accuracy of hydrometeor retrievals. However, the "background hydrometer-dependent" scheme also relies on the accuracy of the background field itself. When the background field is similar to the observation, the "background hydrometer-dependent" method tends to provide accurate hydrometeor weights. On the other hand, when the background field differs significantly from the observation, the algorithm may not be suitable for appropriately allocating hydrometeors of the radar reflectivity observation. Considering their own limitations in either "temperature-based" or "background hydrometer-dependent" schemes, this study aims to adaptively combine two above methods of classifying hydrometeors to assimilate radar reflectivity more reasonably.

134 In the study, the WRF 3DVar methods, observation operators, and different retrieval methods are

included in the section 2. The section 3 shows experimental designs. The section 4 presents analysis

and forecast results of all experiments. The conclusion is presented in the section 5. In the study,

section 2 describes the WRF-3DVar methods, radar observation operators, and a new hydrometeor

138 retrieval method that adaptively combines the "temperature-based" and "background hydrometeor-

139 dependent" methods. Based on two convective cases, three experiments are designed to investigate

the impact of different hydrometeor retrieval schemes on assimilation and prediction, with the

specific configurations presented in section 3. The section 4 presents analysis and forecast results

of all experiments. The conclusion is presented in the section 5.

2. Methods

119

120

121

122

123

124

125

126

127

128

129

130

131

132

133

135

136

137

140

143

144

2.1 The WRF-3DVar system

Based on the incremental method proposed by Courtier et al. (1994), 3DVar uses the minimization algorithm to solve the objective function. The cost function is as follows: **带格式的:**缩进:首行缩进:1字符

148 \mathbf{x}_{b})^T $\mathbf{B}^{-1}(\mathbf{x} - \mathbf{x}_{b}) + \frac{1}{2}[H(\mathbf{x}) - \mathbf{y}_{0}]^{T}\mathbf{R}^{-1}[H(\mathbf{x}) - \mathbf{y}_{0}].$ (1)

147

153

160

168

169

170

171

172

- The vectors $\mathbf{x}_{,\mathbf{x}_{b}}$, and \mathbf{y}_{o} and \mathbf{y}_{o} stand for analysis variables, background variables,
- 150 and observation variables. **B** is the background error covariance, which is calculated by the
- 151 National Meteorological Center (NMC; Parrish and Derber, 1992) method. R represents the
- observation error covariance. *H* is the nonlinear observation operator.

2.2 The radical velocity observation operator

154 The radial velocity observation operator is as follows:

155
$$\frac{V_r}{V_r} = u \frac{x - x_t}{r_t} + v \frac{y - y_t}{r_t} + (w - v_r) \frac{z - z_t}{r_t} \cdot (2) V_r = u \frac{x - x_t}{r_t} + v \frac{y - y_t}{r_t} + v \frac{y -$$

156
$$(w - v_T) \frac{z - z_i}{r_i}$$
 (2)

- 157 u, v, and w denote the zonal, meridional, and vertical wind component, respectively. (x, y, z)
- and (x_i, y_i, z_i) represent the radar position and observation position, respectively. r_i is the
- distance between the radar and the observation. v_T is the terminal speed.

2.3 The radar reflectivity observation operator

161 According to Tong and Xue (2005), the radar reflectivity observation operator is as follows:

$$Z = 10 * \log_{10}(Z_e), \tag{3}$$

163
$$Z_e = Z_e(q_r) + Z_e(q_g) + Z_e(q_g), \tag{4}$$

164
$$Z_e(q_x) = \alpha \mathbf{e}_x (\rho q_x)^{1.75}$$
165 (5

166 q_x means hydrometeor mixing ratios. $Z_e(q_x)$ (units: dBZ) is the equivalent reflectivity factor

of rainwater, snow, and graupel. $\frac{\alpha\alpha_x}{\alpha}$ represents the fixed coefficient that is determined by the

dielectric coefficient, density and intercept parameter of each hydrometeor. α_r is 3.63×10⁹. For

snow and graupel, the coefficient is temperature dependent. When the environmental temperature

is greater than 0°C, α_s for wet snow is 4.26×10^{11} and α_g for wet graupel is 9.08×10^9 . When the

temperature is below 0°C, α_s for dry snow is 9.80×10^8 and α_g for dry graupel is 1.09×10^9 . ρ is

the air density. During the direct assimilation of radar reflectivity, the linearization errors are almost

inevitable. Therefore, the indirect assimilation method is utilized in the study. The indirect method

assimilates the retrieved water vapor and hydrometeors from the radar reflectivity observations.

175 Following Wang et al. (2013), it is assumed that when the radar reflectivity exceeds a certain

176 threshold, the relative humidity reaches 100%. The threshold is set to 30 dBZ in this study. The

177 <u>saturation water vapor at that point is then calculated and assimilated as a pseudo observation,</u>

178 For retrieving hydrometeors from radar reflectivity, The indirect method assimilates the retrieved

179 hydrometeors from the radar reflectivity. Firstly, it is required to determine the proportion of each

180 hydrometeor in radar reflectivity observation. At present, there are two methods to obtain the

181 proportion of each hydrometeor.

186

200

182 2.3.1 The "Temperature-based" method

In Gao and Stensrud (2012), the hydrometeor types in reflectivity are classified based on the

background temperature. The specific values are as follows:

185
$$C_r = 1, C_s = C_g = 0, T_b > 5^{\circ}C,$$
 (6)

$$C_r = \frac{T_b + 5}{10}, C_S = (1 - C_r) \cdot \frac{\alpha_S}{\alpha_S + \alpha_g}, C_g = (1 - C_r) \cdot \frac{\alpha_g}{\alpha_S + \alpha_g}, -5^{\circ}\text{C} < T_b < 5^{\circ}\text{C},$$
 (7)

$$C_r = 0, C_s = \frac{\alpha_s}{\alpha_s + \alpha_g}, C_g = \frac{\alpha_g}{\alpha_s + \alpha_g}, T_b < -5^{\circ}C.$$
 (8)

188 C_r , C_s , and C_g denote the weights of rainwater, snow, and graupel, respectively. α_r , α_s , and

189 α_g represent the fixed coefficients of rainwater, snow, and graupel, respectively (Same as above).

 T_b is the background temperature.

191 2.3.2 The "Background hydrometer-dependent" method

192 It is found that hydrometeor weights derived from the background field vary with individual

193 weather conditions, which helps to reduce errors resulting from fixed coefficients in Chen et al.

194 (2020, 2021). The specific process of calculating proportions is as follows:

195 (1) Compute the average equivalent radar reflectivity of each hydrometeor $(Z_{x(kref_1)})$ in different

reflectivity ranges (ref_i) and model layers (k) based on the background field statistics. The

197 reflectivity ranges are usually set as follows: $ref_1 < 15 \text{ dBZ}$, $15 \text{ dBZ} \le ref_2 < 25 \text{ dBZ}$.

199 (2) Calculate the weight $(C_{x_{(k,ref_i)}})$ of each hydrometeor in the background field. Divide radar

reflectivity observations based on the weights derived from Step 2. If the background field has

设置了格式:字体:(中文)+中文正文(等线)

设置了格式: 字体: 倾斜

带格式的: 列表段落, 多级符号 + 级别: 1 + 编号样式: 1, 2 3, ··· + 起始编号: 1 + 对齐方式: 左侧 + 对齐位置: 0 厘米 + 缩进位置: 0.63 厘米 201 missing data, the calculated climatological mean for one month will be used instead. Cxtkrefti = 202 $\overline{Z_{x_{(k,ref_i)}}}/\overline{Z_{total_{(k,ref_i)}}}$ $\overline{Z_{total_{(k,ref_i)}}} = \overline{Z_{r_{(k,ref_i)}}} + \overline{Z_{s_{(k,ref_i)}}} + \overline{Z_{g_{(k,ref_i)}}}. \tag{10}$ 203 -Divide radar reflectivity observations based on the weights $(\mathcal{C}_{\chi_{(k,ref_i)}})$ derived from Step 2. If 204 205 the background field has missing data, the calculated climatological mean for one month will 206 be used instead. 207 $\frac{(2)}{(3)}$ 设置了格式: 字体颜色: 文字 1 208 2.3.3 The blending method 209 The blending method aims to utilize the two methods of partitioning hydrometeors accordingly 210 to retrieve muti-hydrometer more reasonably in radar reflectivity indirect assimilation. Firstly, 211 calculate the standard deviation σ of each hydrometeor content in the model grid and its 212 surrounding background grids. If the standard deviations of the retrieved hydrometeors of the two 213 schemes are less than 2σ , it means that the retrieved hydrometeors are consistent with the local 设置了格式: 字体颜色: 自动设置 214 structure of the background. Therefore, the hydrometeor content is calculated by the following 215 formulas The formulas are as follow: $\beta = \frac{\delta_t^2}{\delta_t^2 + \delta_h^2},$ 216 217 (911) $C_x = \beta C_x^b + (1 - \beta) C_x^t$ 218 219 (1012)220 δ_t^2 represents the deviation between the hydrometeor content of the background field and the retrieved hydrometeor content based on the "temperature-based" scheme. δ_b^2 is the deviation 221 222 between the hydrometeor content of the background field and the retrieved hydrometeor by the 223 "background hydrometer-dependent" scheme. C_x^t and C_x^b are the weights calculated by the 224 "temperature-based" and "background hydrometer-dependent" methods, respectively. β means the 225 proportion of the results calculated by "background hydrometer-dependent" method. 226 带格式的: 缩进: 首行缩进: 0字符 3. Experimental design 227

WRF v4.3 and its data assimilation system, WRFDA v4.3, are employed in this study. Two-

228

设置了格式:字体: 五号,字体颜色:文字1

convective cases are investigated: 14 June 2020 (referred to as Case 1; Fig. 1a) and 6 August 2018 (denoted as Case 2; Fig. 1b). For Case 1, the model domain consists of 500 × 471 grid points with a horizontal resolution of 3 km and 50 vertical levels. For Case 2, the domain comprises 723 × 691 grid points, also with a 3 km horizontal resolution and 50 vertical levels. The physical parameterizations applied include the WRF Double-Moment 6-Class Microphysics (WDM6) scheme, the Rapid Radiative Transfer Model (RRTM) longwave radiation scheme (Mlawer et al., 1997), the Dudhia shortwave radiation scheme (Dudhia, 1989), the Yonsei University (YSU) boundary layer scheme (Hong et al., 2006), and the Noah Land Surface Model (Chen and Dudhia, 2001) for land surface processes. No cumulus parameterization scheme is used. As summarized in Table 1, three data assimilation (DA) experiments are conducted to evaluate the effects of all retrieval methods considered in this study. For all three DA experiments, the initial and lateral boundary conditions are provided by NCEP Global Forecast System (GFS) data. Additionally, the specific workflow is illustrated in Fig. 2. Radar observations for both cases undergo a series of preprocessing and quality control procedures, including anomaly detection and velocity de-aliasing. The observation errors for radar radial velocity and radar reflectivity are set to 2 m s⁻¹ and 5 dBZ, respectively, WRF v4.3 and its data assimilation system WRFDA v4.3 are used in this study. Two convective cases are studied in the study: 14 June in 2020 (called Case 1; Fig. 1a) and 6 August in 2018 (denoted as Case 2; Fig. 1b). For case 1, the model domain contains 500×471 with a 3 km horizontal grid spacing, and 50 vertical levels. For case 2, the model domain contains 723 × 691 with a 3 km horizontal grid spacing, and 50 vertical levels. The specific applications of physical parametrizations are as follows: the WRF Double Moment 6 Class Microphysics (WDM6) scheme, the Rapid Radiative Transfer Model (RRTM) long wave radiation scheme (Mlawer et al., 1997), the Dudhia short wave radiation scheme (Dudhia, 1989), the Yonsei University (YSU) boundary layer scheme (Hong et al., 2006), and the Noah Land Surface Model (Chen and Dudhia, 2001) for land surface process scheme. No cumulus parameterization scheme is employed. As shown in Table 1, three data assimilation (DA) experiments are conducted to evaluate the effects of all retrieval methods in the study. For all three DA experiments, the initial and lateral boundary conditions are provided by the NCEP Global Forecast System (GFS) data. Besides, the specific flowchart is presented in the Fig. 2. The radar observations used in two cases undergo a series of preprocessing

229

230

231

232

233

234

235

236

237

238

239

240

241

242

243

244

245

246

247

248

249

250

251

252

253

254

255

256

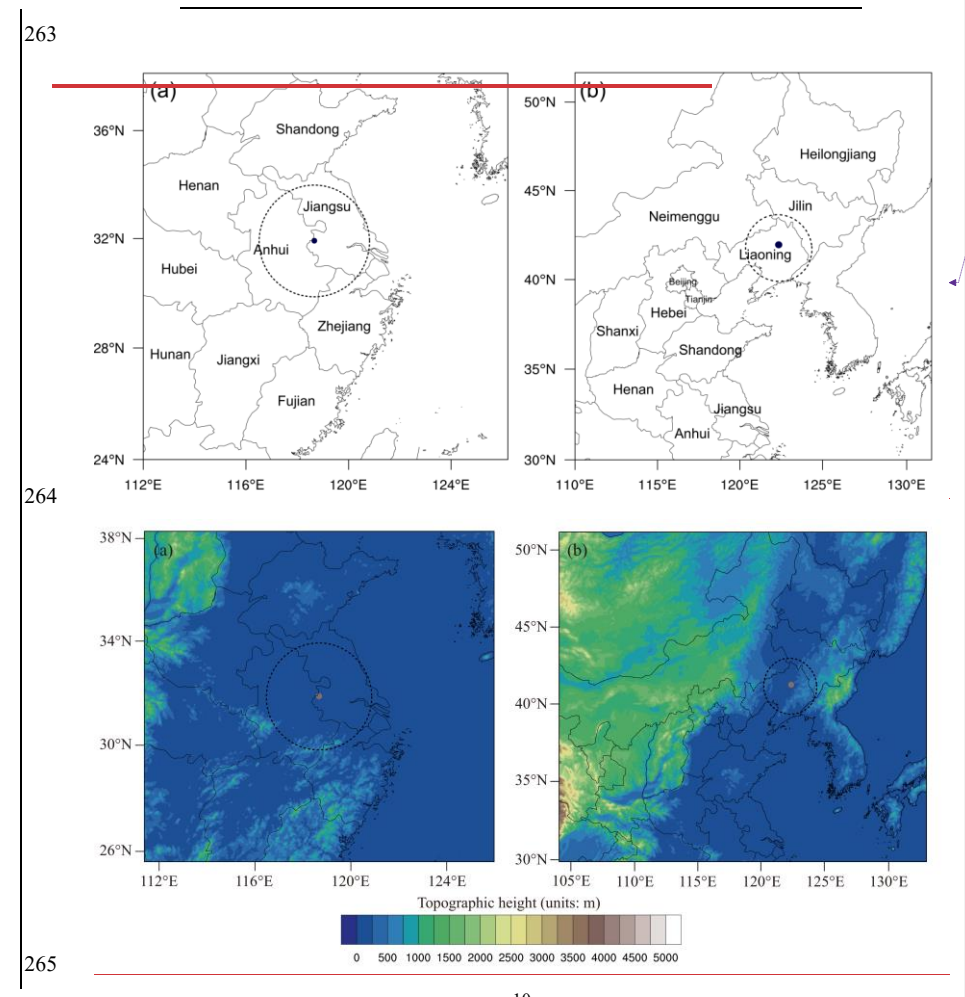
257

设置了格式: 字体: 五号

and quality control procedure, including anomaly detection, velocity de-aliasing, and so on. The observation errors of radar radial velocity and radar reflectivity are set to 2 m s⁻¹-and 5 dBZ, respectively.

Table 1. The list of DA experiments.

Experiments	Hydrometeor retrieval methods
EXP_temp	The "temperature-based" method
EXP_bg	The "background hydrometer-dependent" method
EXP_temp-bg	The blending method



269270

271

272273

274

275

276

277278

279

280

281

282

Fig. 1. The simulated area of (a) Case 1 and (b) Case 2, with the detecting ranges of the Nanjing radar and Shenyang

Radar. Both radars are S-band Doppler radars with a maximum coverage range of 230 km. The radial velocity and

reflectivity observations have range resolutions of 250 m and 1000 m, respectively.

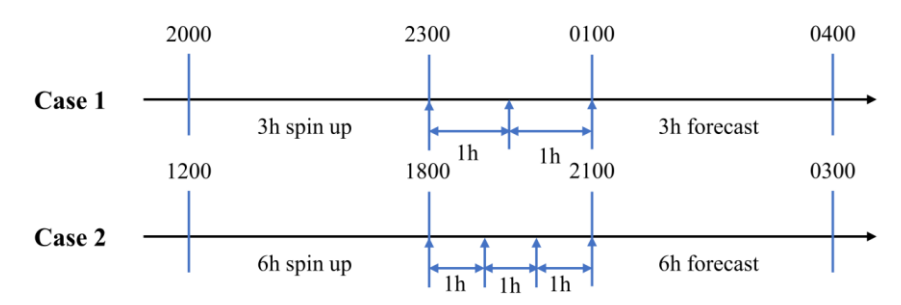
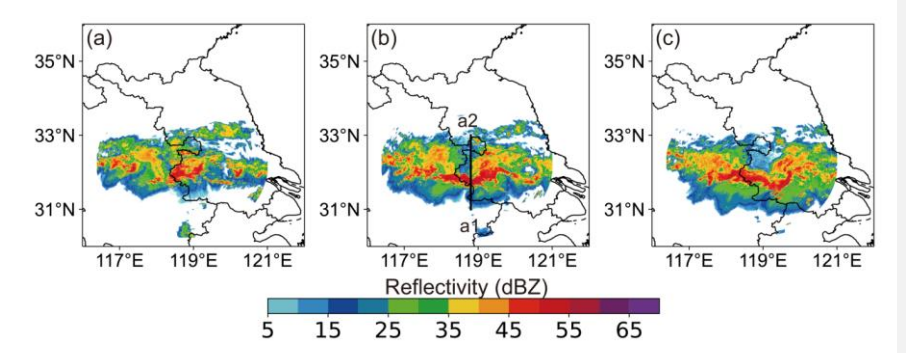


Fig. 2. The assimilation flow charts of Case 1 and Case 2.

4. Experimental results

4.1 14 June 2020 case

Fig. 3 shows the observed reflectivity at 2300 UTC on 14 June, 0000 UTC, and 0100 UTC on 15 June 2020. At the beginning, there are strong echoes in the southwestern boundary of Jiangsu Province. Subsequently, the strong convective band begins to expand in both eastward and westward directions, stretching to the central Anhui Province and Jiangsu Province.

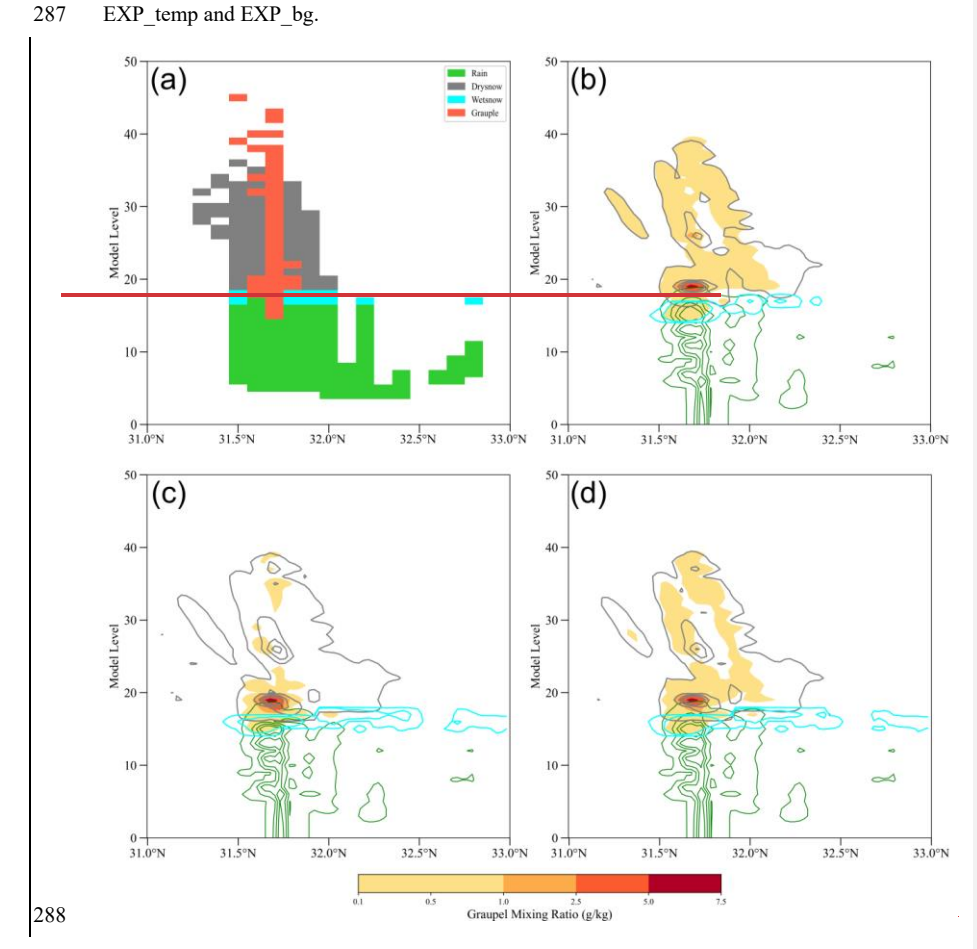


 $Fig.\ 3.\ The\ observed\ composite\ reflectivity\ fields\ (units:\ dBZ)\ at\ (a)\ 2300\ UTC\ 14\ June,\ (b)\ 0000\ UTC,\ and\ (c)$

 $0100\ \mathrm{UTC}\ 15\ \mathrm{June}\ 2020.$ The black line a1-a2 in the Fig. 3b is the vertical cross section location of Fig. 4.

Fig. 4 compares the Hydrometeor Classification Algorithm (HCA) based on dual-polarization radar observations with the hydrometeor retrieval results from the three experiments at 1500 UTC on June 14, 2020. The HCA diagram indicates that rainwater dominates the lower levels, while dry

snow and graupel prevail at higher levels, with wet snow present near the melting layer. In the vertical cross sections of the three experiments (Figs. 4b, c, d), the overall distribution patterns of the retrieved hydrometeors appear reasonable, especially for rain and snow. Notably, the wet snow and graupel retrieved by EXP_temp-bg are more consistent with the HCA results compared to EXP_temp and EXP_bg.



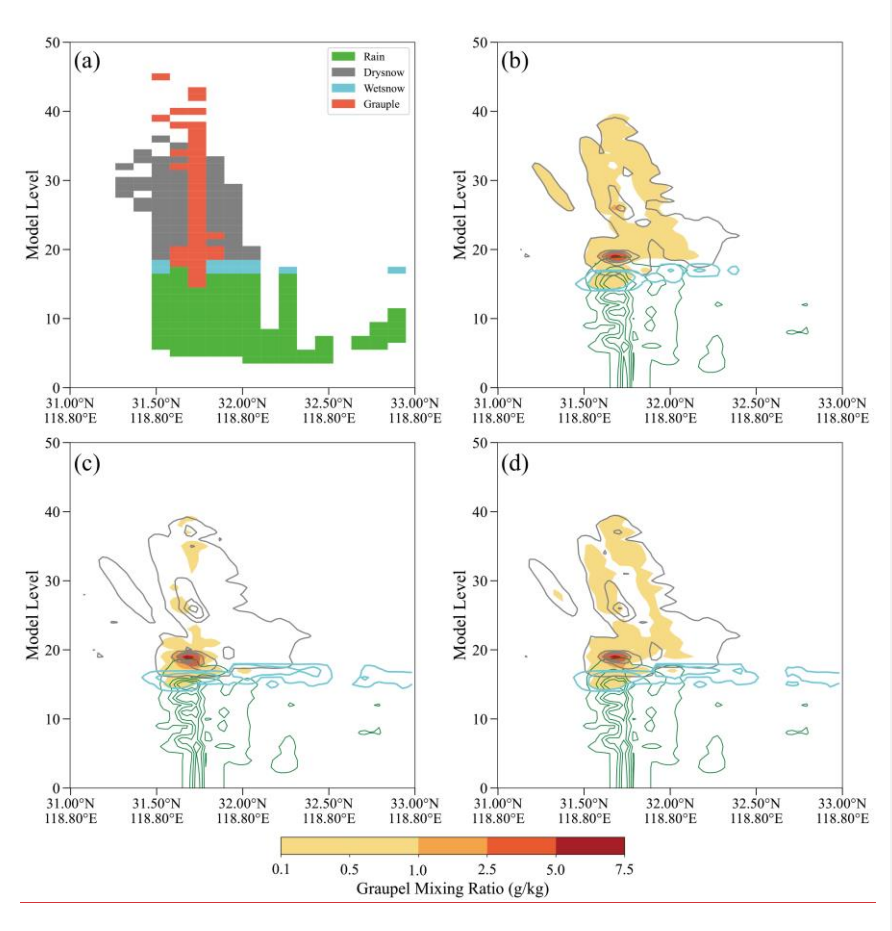
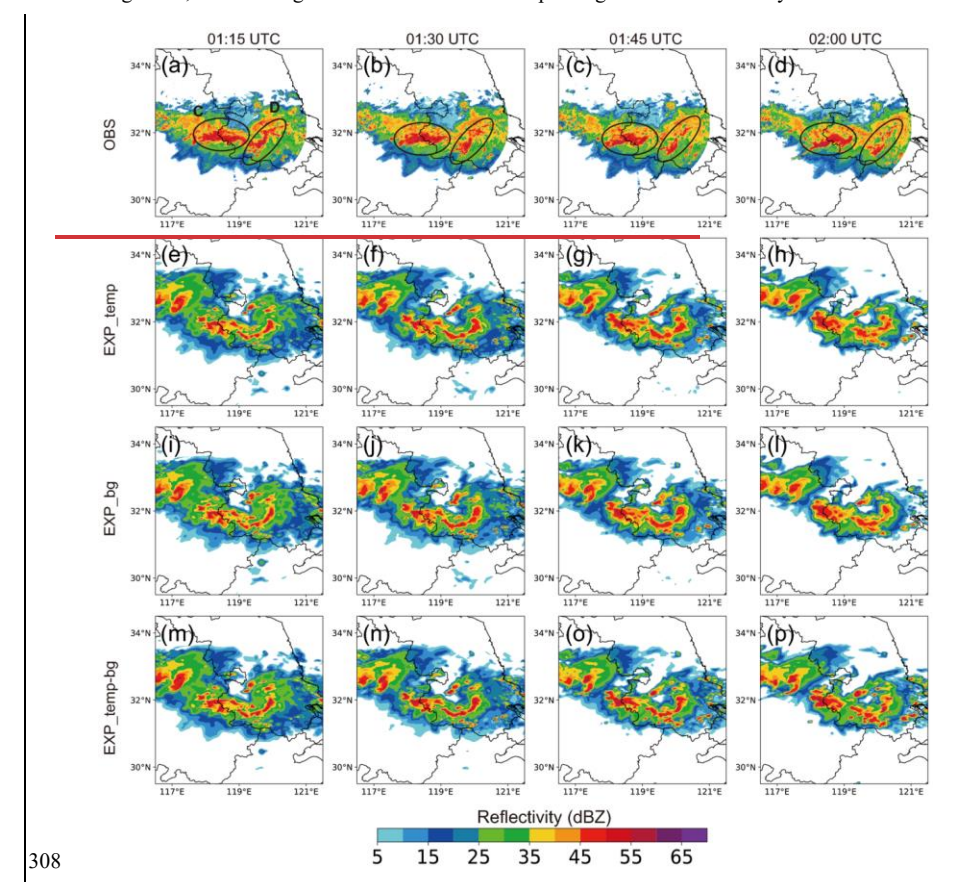


Fig. 4. The vertical sections of (a) hydrometeor classification algorithm based on the dual-polarization radar observations and retrieved hydrometeors for (b) EXP_temp, (c) EXP_bg and (d) EXP_temp-bg along the black lines a1-a2 at 1500 UTC. The retrieved hydrometeors refer to rainwater mixing ratio (green contours; units: dBZ), dry snow mixing ratio (grey contours; units: dBZ), wet snow mixing ratio (cyan contours; units: dBZ), and graupel mixing ratio (shading; units: dBZ), respectively.

To investigate the impact of the radar reflectivity DA based on the three hydrometeor retrieval methods, Fig. 5 shows the predicted composite reflectivity initiated at 0100 UTC 15 June. It is shown that the convective structure is divided into two parts (labeled C and D). From the observations (Fig. 3a), the combination of C and D is initially located in the western Jiangsu and eastern Anhui. Soon after, region D gradually separates from C and shifts eastward, displaying the reduced intensity and poor organization. At 0115 UTC, all DA experiments are able to capture region

C and region D, albeit with slightly weaker intensity compared to the observations. At 0130 UTC, the patterns of region C predicted by three experiments are depart from the observation, while the echoes for EXP_temp-bg exhibit the best organization. At 0145 UTC, the regions C in EXP_temp and EXP_bg show a poor agreement with the observations. In contrast, EXP_temp-bg provides more accurate forecast in terms of shape and intensity. At 0200 UTC, three experiments can predict region C and region D to some extent, but region D in EXP_temp-bg has most accurate echo pattern. In general, the blending scheme is conducive to improving the radar reflectivity forecast skill.



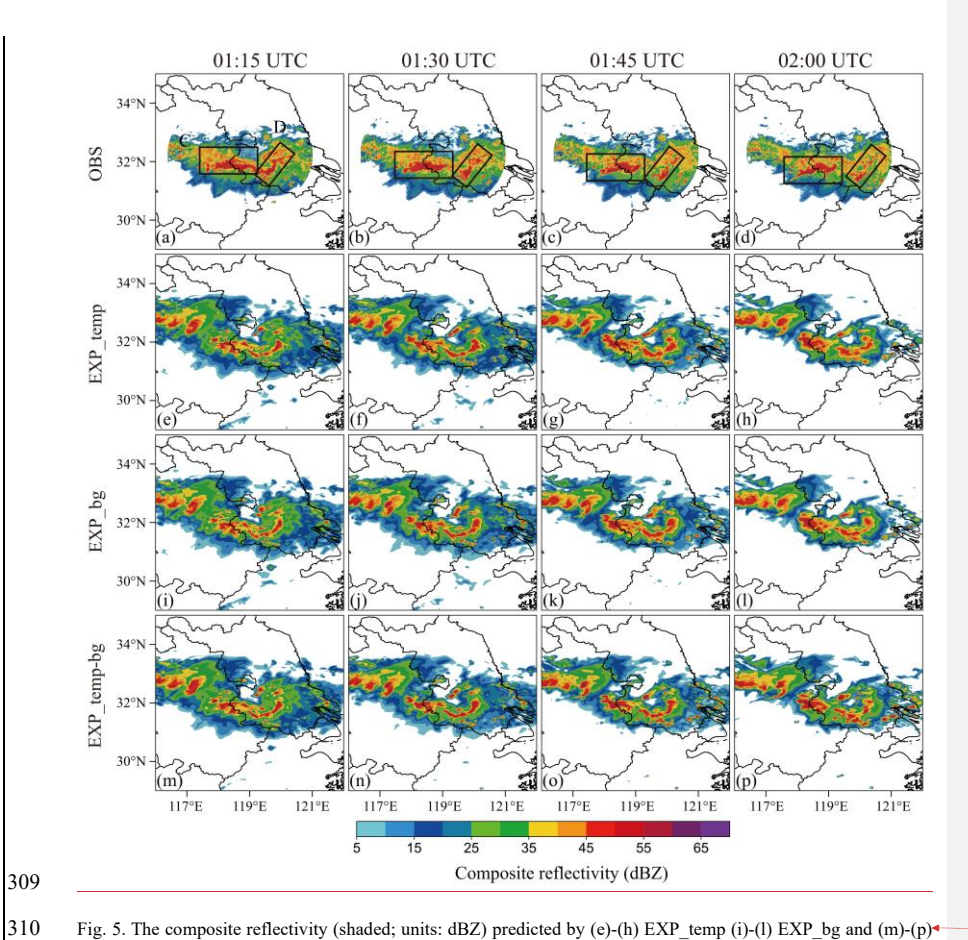


Fig. 5. The composite reflectivity (shaded; units: dBZ) predicted by (e)-(h) EXP_temp (i)-(l) EXP_bg and (m)-(p) EXP_temp-bg for the 1-h forecast beginning at 0100 UTC 15 June 2020, as compared to (a)-(d) the observed

composite reflectivity. The labels C and D present the convection locations.

Fig. 6 displays the vertical cross sections of the relative humidity, radar reflectivity, and wind fields at 1501 UTC. After 1-hour forecast, the cross sections from all experiments indicate the presence of saturated water vapor columns near the strong echoes (around 32°N). Notably, EXP_temp-bg also reveals a robust updraft, facilitating the transport of water vapor from lower to upper levels. In comparison, EXP_temp-bg producess the most consistent thermal and dynamical conditions, resulting in most accurate forecast of the convection.

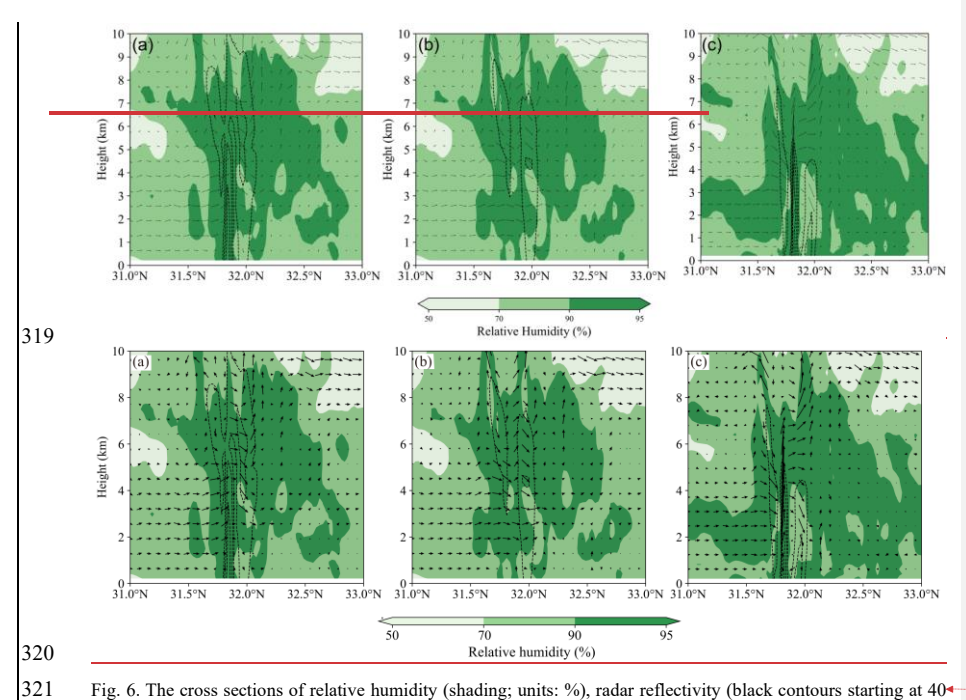
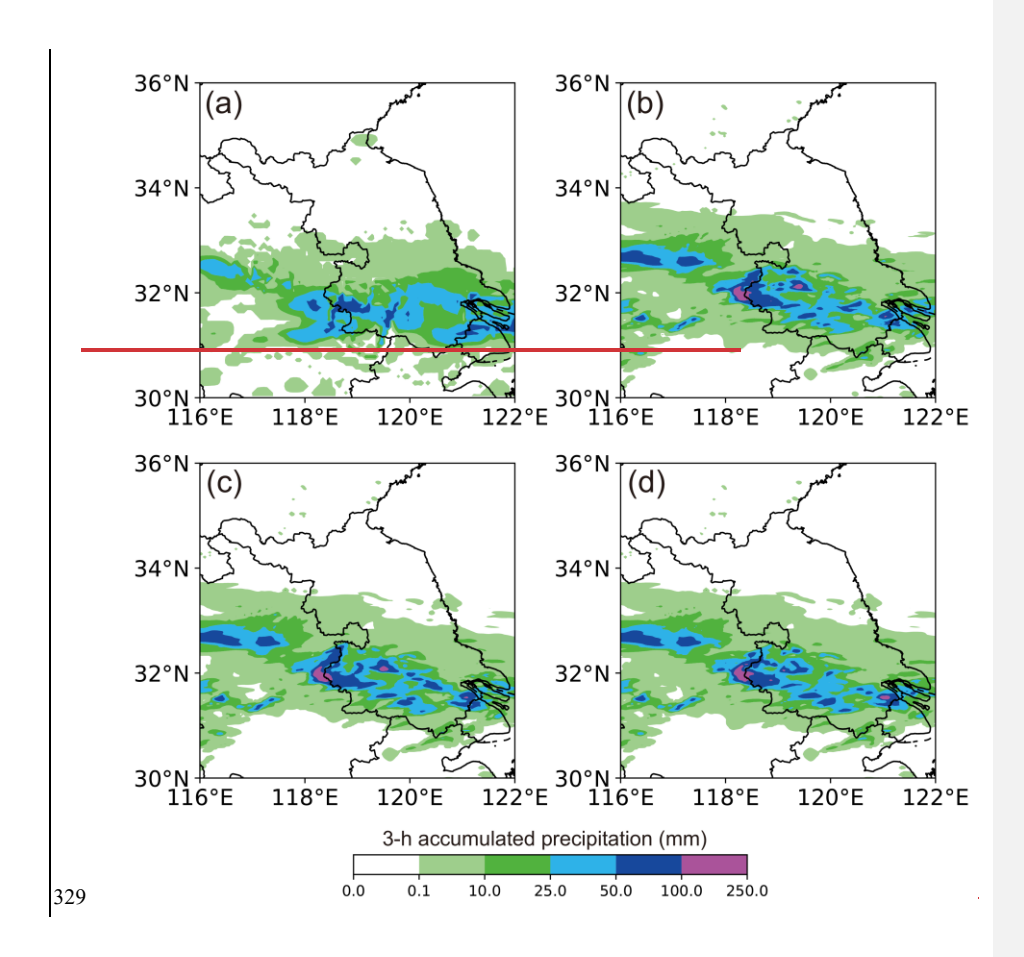


Fig. 6. The cross sections of relative humidity (shading; units: %), radar reflectivity (black contours starting at 40 dBZ; units: dBZ), and wind vectors for (a) EXP_temp, (b) EXP_bg and (c) EXP_temp-bg along the line a1-a2. These are 1-hour forecasts initialized at 1501 UTC.

Fig. 7 shows the 3-h accumulated precipitation forecast from 1501 UTC to 1504 UTC on 15 June 2020. As depicted in Fig. 7a, the primary precipitation zone is concentrated along the western boundary of Jiangsu Province, with accumulated precipitation exceeding 50mm. The precipitation intensity is overestimated for three DA experiments. However, EXP_temp-bg effectively suppresses two false precipitation areas, leading to the improved precipitation forecast.



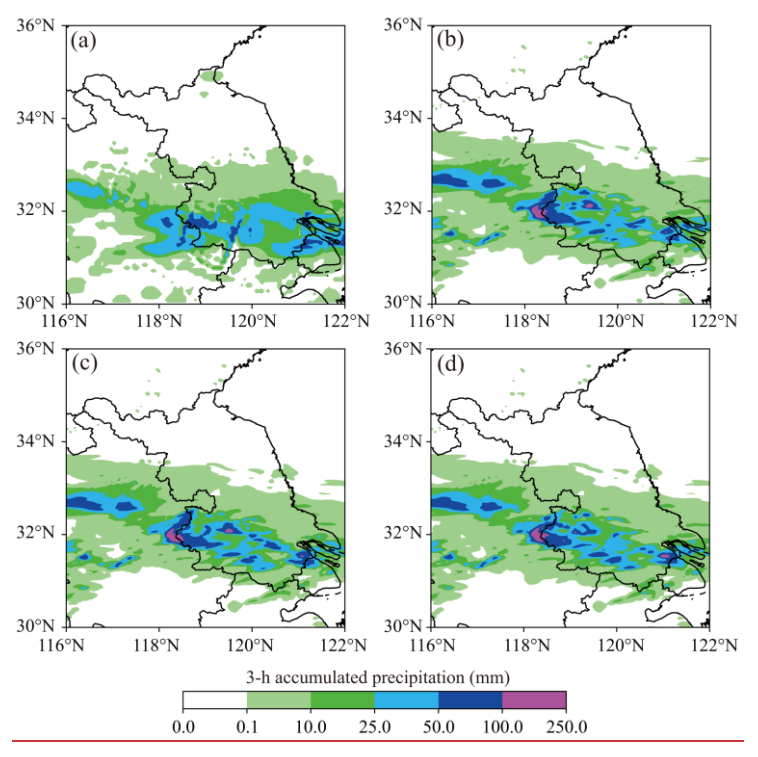


Fig. 7. 3-h accumulated precipitation initialized valid at 0100 UTC 15 June 2020. (a) the observation, (b) EXP_temp,

(c) EXP_bg, and (d) EXP_temp-bg.

To quantitatively assess the performance of different hydrometeor retrieval schemes, the equitable threat scores (ETS) are calculated for 0-3 h precipitation forecasts in EXP_temp, EXP_bg, and

EXP_temp-bg (Fig. 8). The specific calculation formula of ETS is as follows:

$$ETS = \frac{A-R}{A+B+C-R^2}.$$

$$R = \frac{(A+C)\times(A+B)}{A+B+C+D}.$$
(14)

where A, B, C, and D are the number of hits, the false alarms, the misses, and the correct negatives. The R means the probability to have a correct forecast by chance.

It is evident that as the precipitation threshold increases, the ETS values for all three experiments decline progressively. Furthermore, EXP_temp and EXP_bg exhibit comparable ETS values under various precipitation thresholds. In contrast, EXP_temp-bg consistently outperforms both EXP_temp and EXP_bg for the entire 3-h forecast period, which implies that the integrated

带格式的: 两端对齐

设置了格式: 字体: 五号, 字体颜色: 自动设置设置了格式: 字体: 五号, 字体颜色: 自动设置带格式的: 缩进: 首行缩进: 16 字符设置了格式: 字体: 五号, 字体颜色: 自动设置设置了格式: 字体: 五号, 字体颜色: 自动设置

344 hydrometeor retrieval scheme is conducive to the assimilation of radar reflectivity observations.

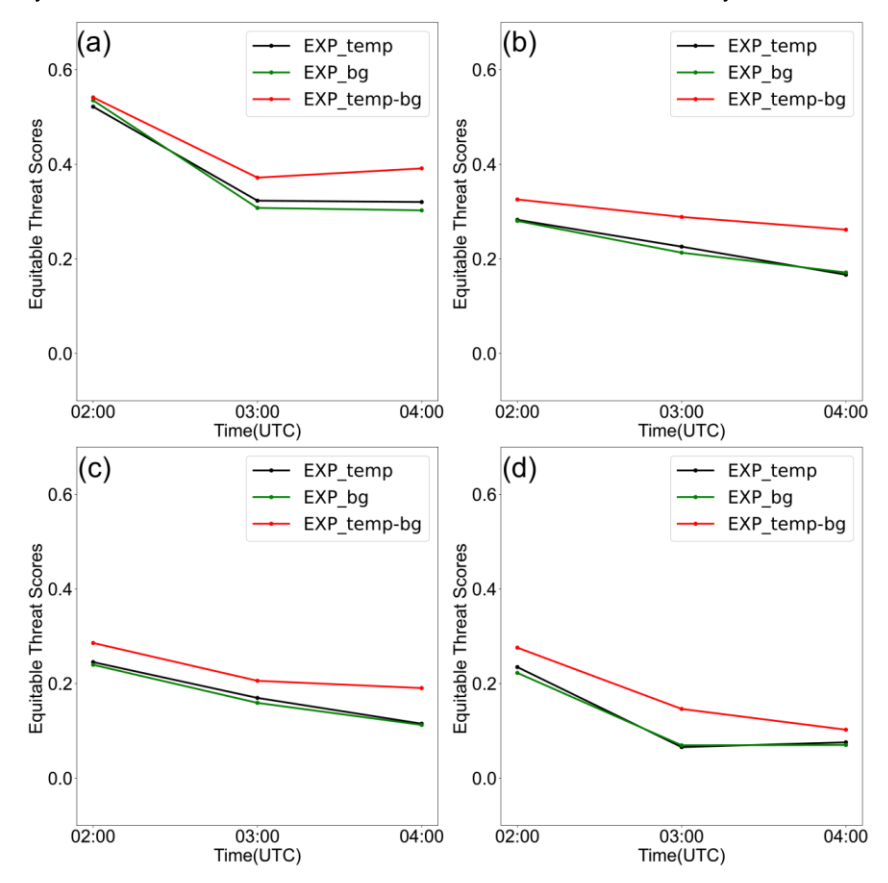


Fig. 8. Equitable threat scores of hourly accumulated precipitation forecasts with five thresholds: (a) 0.1 mm, (b) 2.5 mm, (c) 5 mm and (d) 10 mm from 2300 UTC 14 June to 0100 UTC 15 June.

带格式的: 两端对齐

4.2 06 August 2018 case

Fig. 9 presents the observed composite reflectivity at 1800UTC, 1900UTC, 2000UTC, and 2100UTC on 06 August 2018. At 1800 UTC, there are a small number of strong radar echoes in the central part of Liaoning Province. At 1900UTC, these discrete strong echoes gradually converge in the center Liaoning, forming a well-organized structure. By 2000UTC, the convections continue to develop and form into "V" pattern echo. At 2100UTC, a distinct "T" shaped echo emerges in the observed area.

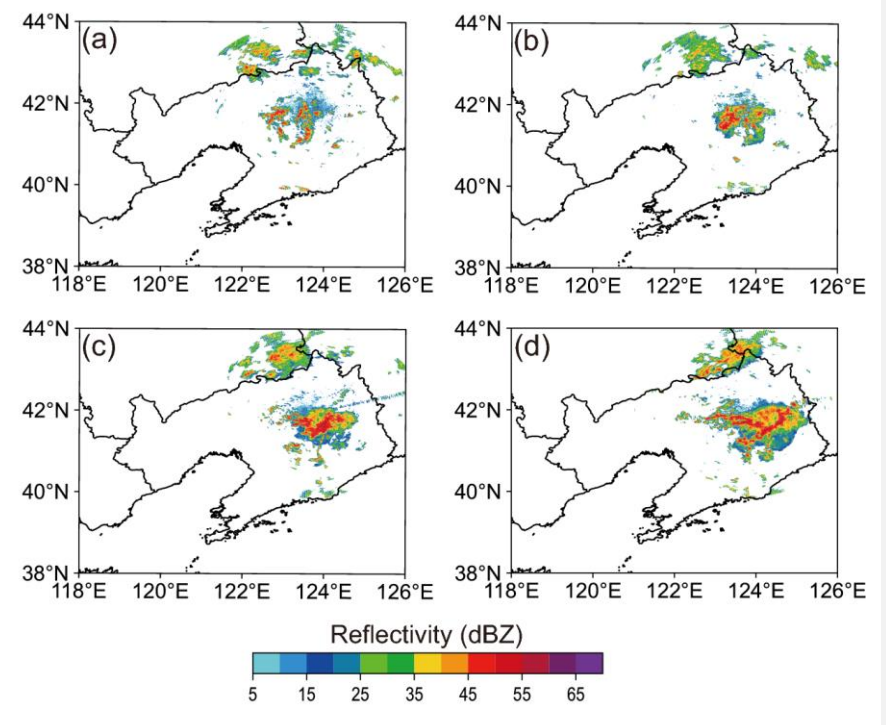
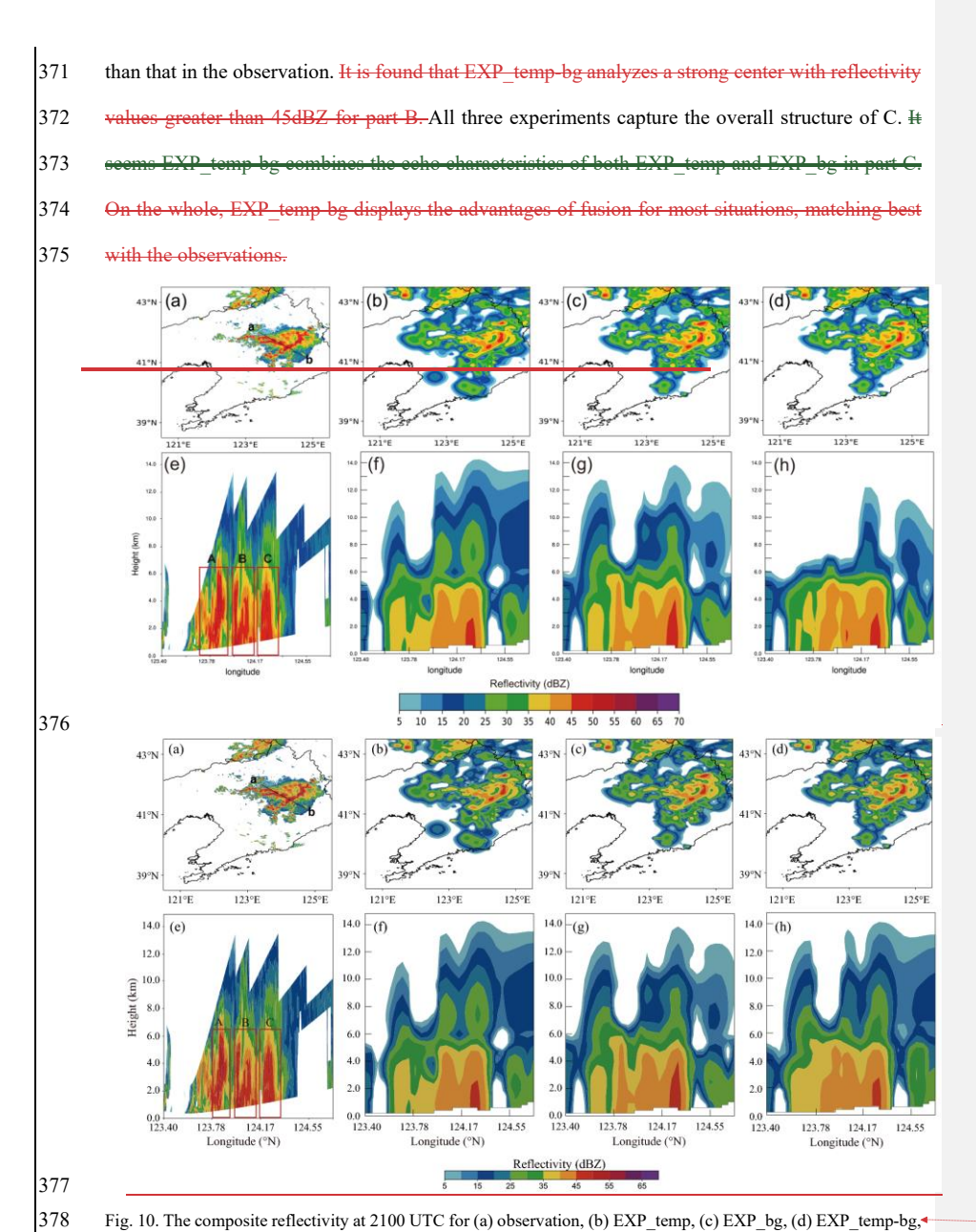


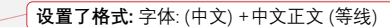
Fig. 9. The observed composite reflectivity fields (units: dBZ) at (a) 1800UTC, (b) 1900UTC, (c) 2000UTC and (d) 2100UTC 06 August 2018.

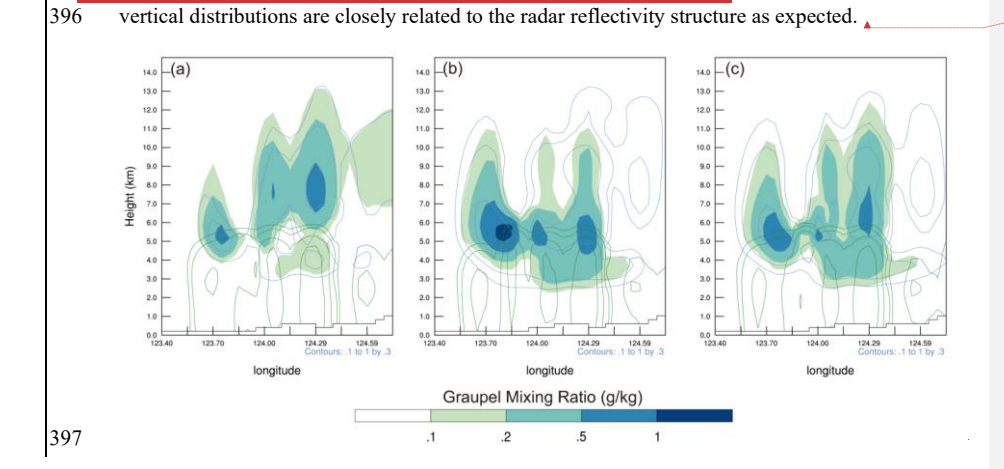
 Fig. 10 shows the radar reflectivity analysis fields and the vertical cross sections along the line ab from EXP_temp, EXP_bg, and EXP_temp-bg at 2100 UTC. As shown in Fig. 10a, a distinct "T" shaped echo emerges in the observed area. Generally, the composite reflectivity analyses of the experiments EXP_temp, EXP_bg, and EXP_temp-bg show a general agreement. From the observed vertical cross section, it seems that there exist three strong echo bands between 123.78°E and 124.36°E. In order to display the differences between three DA experiments and the observation, the convective system located near 123.75°E is marked as A, the strong convection at 123.97°E - 124.17°E is named as B, and the strong echo region at 124.17°E -124. 36°E is labelled as C. Notably, part A in the experiment EXP_temp departs from the observation, while EXP_bg and EXP_temp-bg capture it more closely. It seems EXP temp-bg combines the echo characteristics of both EXP_temp and EXP_bg in part CA_Furtherly, the strong echo band analyzed by EXP_temp-bg indicates a wider coverage than the one obtained from EXP_bg in part A_For part B, though all three DA experiments exhibit a general agreement with the observation, their intensity is weaker



accompanied by the vertical cross sections for (e) observation, (f) EXP_temp, (g) EXP_bg, (h) EXP_temp-bg along the line ab. The vertical cross section location at 2100UTC is shown by the line ab in the Fig. 10a. The labels in the Fig. 10e present the convection locations.

To examine how different retrieval methods modify the hydrometeor distributions, the rainwater, snow and graupel mixing ratio cross sections are presented in Fig. 11. Rainwater occurs below the freezing level, while snow and graupel particles primarily exist above the freezing level. The distribution of low-level rainwater in EXP_temp-bg is similar to that in EXP_bg. The proportion of snow and graupel is a fixed coefficient in the EXP_temp, resulting in similar vertical distributions as shown in Fig. 11a. FHowever, or schemes associated with the background, the weights assigned to different hydrometeors vary dynamically with the background field. Therefore, it—the fixed coefficient does not exist in the other two experiments (EXP_bg and EXP_temp-bg) with the "background hydrometer-dependent" scheme. Additionally, both EXP_bg and EXP_temp-bg have significantly higher snow and graupel content than EXP_temp. Fig. 11 shows three strong centers of graupel particles corresponding to three strong reflectivity bands in the Fig. 10. By comparing the three groups of the DA experiments, it is apparent that EXP_bg has the highest strong-center value, while EXP_temp has the lowest. Moreover, the distribution of high-altitude hydrometeors in EXP_temp-bg combines the features of EXP_temp and EXP_bg. To conclude, the hydrometeor





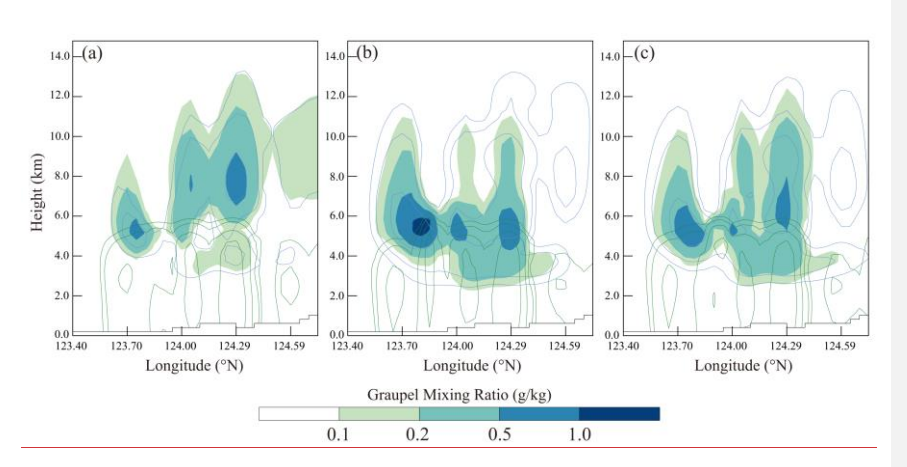


Fig. 11. The vertical cross sections of rainwater mixing ratio (green contours), snow mixing ratio (blue contours), graupel mixing ratio (shading) at 2100 UTC for the experiments (a) EXP_temp, (b) EXP_bg, (c) EXP_temp-bg. The position of the cross sections is located at the line ab of the Fig. 10a.

Fig. 12 displays the vertical cross sections of the pseudo-equivalent potential temperature (θse), wind components, and reflectivity at 2100 UTC for EXP_temp, EXP_bg, and EXP_temp-bg. In the three DA experiments, there exists a high θse zone in the lower layers (below 3 km), which shows that a certain amount of energy has accumulated near the ground level. The area between 3 and 9 kilometers is characterized by a low θse zone, with the lowest value being below 343 K. Another high θse zone exists above 10 kilometers. All three data assimilation (DA) experiments exhibit a high-low-high vertical distribution of θse. The results It suggests that the vertical structure of the atmosphere is unstable in this region, with dry conditions prevailing in the upper levels and moist conditions in the lower levels. This type of vertical structure is favorable for the development of severe convective weather events.

In the middle layer, there is a zone with relatively high θse value for EXP_bg and EXP_temp-bg. Specifically, a warm-core structure is identified near 123.85°N, accompanied by strong upward motion. This results in the release of unstable energy indicate that a severe convective system is continuously developing. Additionally, compared with EXP_bg, EXP_temp-bg yields a more extensive and deeper updraft column.

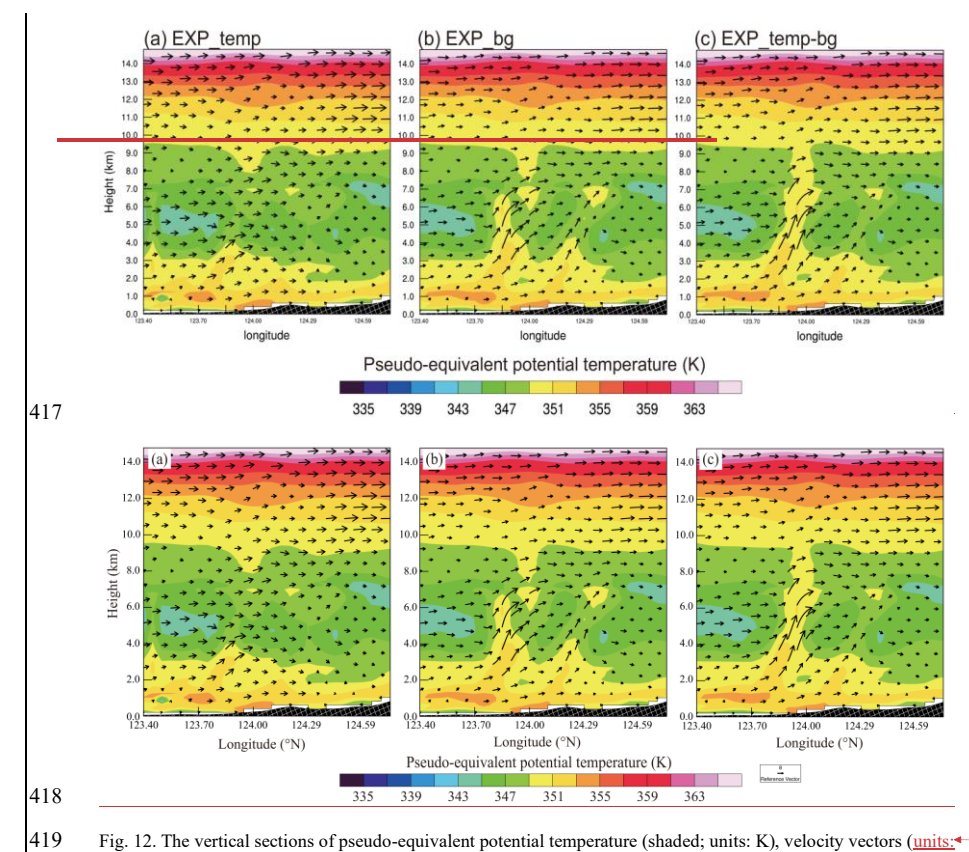
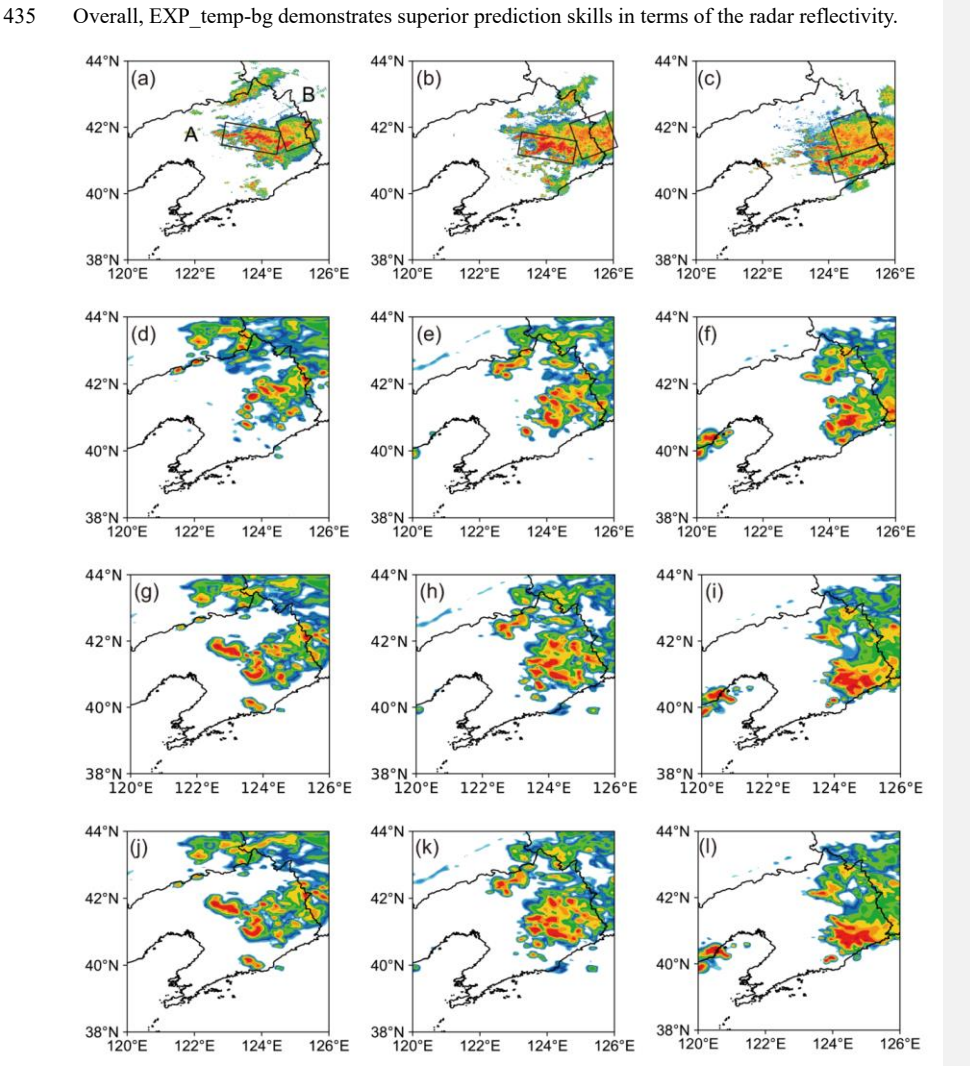


Fig. 12. The vertical sections of pseudo-equivalent potential temperature (shaded; units: K), velocity vectors (units: m/s; the vertical velocity has been multiplied by 10U, W) at 2100 UTC for (a) EXP_temp, (b) EXP_bg and (c) EXP_temp-bg. The position of the cross sections is located at the line ab of the Fig. 10a.

Fig. 13 shows 1-h, 3-h, and 5-h forecasts initialized_valid_at 2100 UTC 06 August 2018 for EXP_temp, EXP_bg, and EXP_temp-bg. As can be seen from the observation, the strong echo is located near 42°N at the beginning and has a tendency to slowly develop to the east. For the sake of clarity, the strong echo zone is divided into two parts: part A and part B. At 2200 UTC 06 August, the forecasts of three DA experiments for part B are inconsistent with the observation in terms of the intensity. The part A predicted by EXP_bg and EXP_temp-bg shows a general agreement with the observation, while the radar reflectivity forecast of EXP_temp departs from the observation. At 0000 UTC 07 August, EXP_bg and EXP_temp-bg yield an improved forecast for part A and B as compared with EXP_temp, in terms of the intensity and organization. However, there is a southeast bias in part A predicted by both EXP_bg and EXP_temp-bg. Compared to EXP_bg, EXP_temp-bg

provides more accurate predictions for part B. As shown by the observation at 0200 UTC 07 August, the predicted A in EXP_temp-bg shows closer alignment with the observation than that in EXP_temp and EXP_bg. For part B, three sets of experiments all depart from the observation. Overall, EXP_temp-bg demonstrates superior prediction skills in terms of the radar reflectivity.



 $Fig. \ 13. \ The \ composite \ reflectivity \ (shaded; \ units: \ dBZ) \ predicted \ by \ (d)-(f) \ EXP_temp \ (g)-(i) \ EXP_bg \ and \ (j)-(l) \ denote \ (g)-(l) \ denote \ (g)-(l)$

Reflectivity (dBZ)

EXP_temp-bg, as compared to (a)-(c) the observed composite reflectivity. The corresponding times from left to right are 2200 UTC 06 August (left), 0000 UTC 07 August (middle) and at 0200 UTC 07 August (right), respectively. The labels A and B present the convection locations.

Fig. 14 shows 6-h accumulated precipitation of the three DA experiments from 2100 UTC 06 August to 0300 UTC 07 August 2018. According to the observation, heavy rainfall is mainly concentrated in the northeastern part of Liaoning, with precipitation amount exceeding 100 mm. All three experiments underestimate the extent of the precipitation in this event, especially in the range of 25 mm to 50 mm. Moreover, there is a certain deviation between the predicted and observed locations. As shown in Fig. 149c and d, the patterns of heavy precipitation areas are similar in EXP_bg and EXP_temp-bg. EXP_bg and EXP_temp-bg are notably better than EXP_temp in predicting the rainfall for the threshold 50mm. EXP_temp-bg displays the best forecasting skill in terms of the heavy rainfall area.

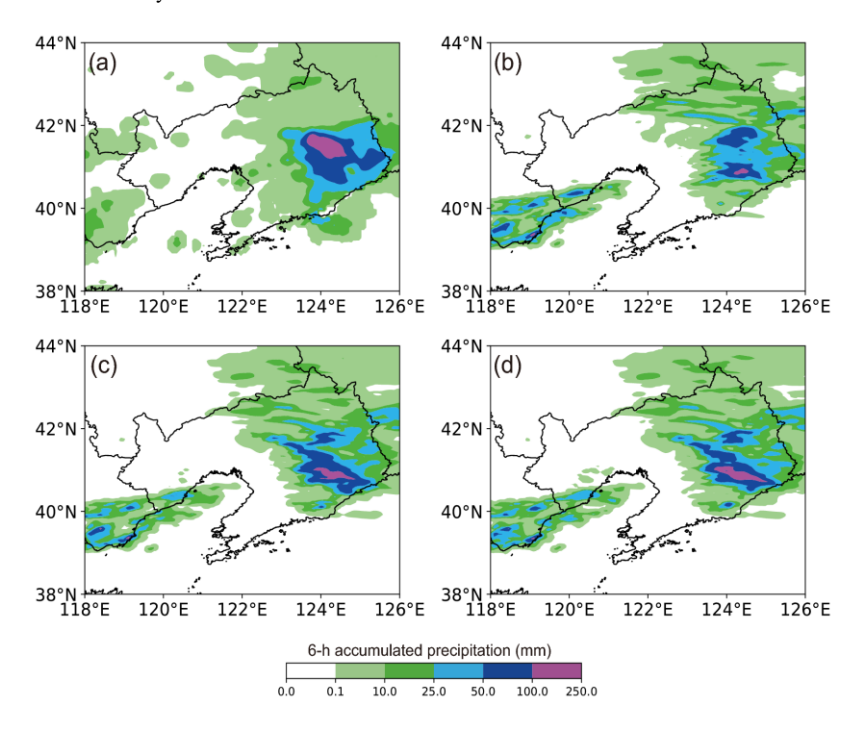


Fig. 14. 6-h accumulated precipitation initialized at 2100 UTC 06 August 2018. (a) the observation, (b)

EXP_temp, (c) EXP_bg, and (d) EXP_temp-bg

Figure 15 shows ETS values of 1-h accumulated precipitation for EXP temp, EXP bg, and

设置了格式: 字体: 小五

带格式的: 缩进: 首行缩进: 1字符

EXP_temp-bg. For the threshold of 2.5 mm/h, the precipitation forecasts of EXP_temp-bg generally exhibit superior quality. The EXP_temp experiment consistently shows the lowest ETS scores among the three experiments. At the threshold of 10 mm/h, the ETS score of EXP_temp-bg gradually increases in the later stages of the forecast. These results indicate that the blending method is able to improve precipitation forecast skill. Fig. 15 shows ETS values of 1-h accumulated precipitation for EXP_temp, EXP_bg, and EXP_temp bg. For the thresholds of 2.5 mm/h, the precipitation forecasts of EXP_temp-bg generally exhibit superior quality. The experiment EXP_temp keeps the worst for the ETS scores among the three sets of experiments. At thresholds of 10 mm/h, the score of EXP_temp-bg gradually increases in the later stage of forecast. The scores indicat that the blending method is able to improve the precipitation forecast skill.

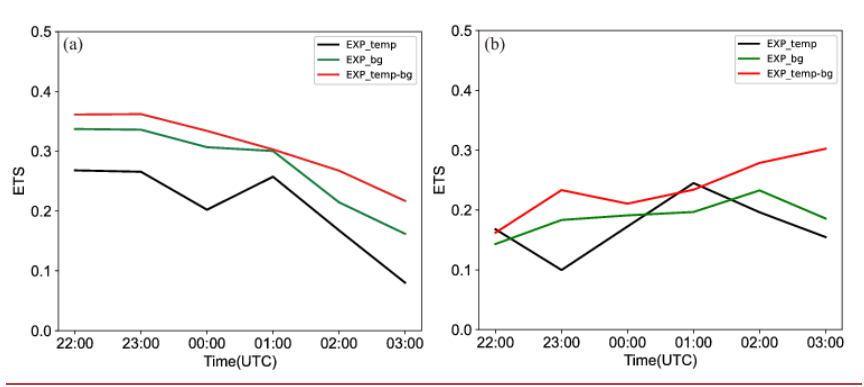


Fig. 15. ETS of three DA experiments for the thresholds of (a)1mm/h, (b)3mm/h and (c)5mm/h,

5. The conclusion

The study proposes an adaptive hydrometeor retrieval scheme within the WRF-3DVar system, which combines "temperature-based" and "background hydrometer-dependent" methods to enhance the analyses and forecasts for the strong convections. In the indirect assimilation of radar reflectivity, it is vital to correctly divide hydrometeor information in radar reflectivity. On the basis of two retrieval methods proposed by Gao and Stensrud (2012) and Chen et al. (2020, 2021), the blending scheme is developed to minimize the limitations brought by both methods so as to improve the assimilation and prediction skills.

The above three hydrometeor retrieval schemes are evaluated for two strong convective processes occurred during June 2020 and August 2018. Three DA experiments (EXP_temp, EXP_bg, and

设置了格式: 字体: 五号

设置了格式: 字体: 小五

设置了格式:字体:(中文)+中文正文(等线)

EXP temp-bg) are conducted by using the "temperature-based", "background hydrometerdependent", and blending methods, respectively. The analysis results reveal that the blending method is effective to improve the radar reflectivity structures for severe convections. Based on the other two DA experiments, EXP temp-bg further improves hydrometeor structures and properly allocates the proportion of each hydrometeor, which is responsible for more reasonable hydrometeor distributions. Also, EXP_temp-bg provides more reasonable dynamic and thermal structures compared with EXP temp and EXP bg. EXP temp-bg shows advantages in the precipitation prediction skills due to the reasonable spatial distribution and proportion of each hydrometeor. Compared to conventional Doppler weather radars, dual-polarization radar observations provide more accurate identification of the three-dimensional microphysical structures within precipitation systems. Consequently, dual-polarization radar data (e.g. differential reflectivity, specific differential phase, correlation coefficient) will be considered for identifying the hydrometeor types more accurately hydrometeor retrievals in our future studies, aiming to further enhance the

489 490 491

494

495

476

477

478

479

480 481

482

483

484

485

486

487

488

Data availability

492 The GFS reanalysis data is available at https://rda.ucar.edu/datasets/ds084.1/, and the source code 493

effectiveness of radar data assimilationenhance the forecast skills for severe weathers.

of WRF and WRFDA can be downloaded from https://github.com/wrf-model. The radar

observations after quality control are provided by Jiangsu and Liaoning Provincial Meteorological

Bureau. and the precipitation observations found

496 http://data.cma.cn/dataService/cdcindex/datacode/NAFP CLDAS2.0 NRT/show value/normal.ht

497 <u>ml</u>.

498 499

501

502

Author contribution

500 LS: visualization, writing (original draft). FS: conceptualization, writing (review and editing). ZH:

conceptualization, methodology. DX: writing (review and editing). AS: visualization. JC: software.

Competing interests 503

504 The contact author has declared that none of the authors has any competing interests.

505	
506	Acknowledgments
507	This research was primarily supported by National Key R&D Program of China (2024YFC2815702),
508	Key Laboratory of Urban Meteorology, China Meteorological Administration, Beijing (LUM-2025-02),
509	the China Meteorological Administration Tornado Key Laboratory (TKL202306), Natural Science Fund
510	of Anhui Province of China under grant (2308085MD127), the Open Grants of China Meteorological
511	Administration Radar Meteorology Key Laboratory (2023LRM-B03), the Open Project Fund of China
512	Meteorological Administration Basin Heavy Rainfall Key Laboratory (2023BHR Y20), the Shanghai
513	Typhoon Research Foundation (TFJJ202107), the Chinese National Natural Science Foundation of China
514	(G41805070). We acknowledge the High Performance Computing Center of Nanjing University of
515	Information Science & Technology for their support of this work.
516	References
517	Bick, T., Simmer, C., Trömel, S., et al. 2016: Assimilation of 3D radar reflectivities with an ensemble
518	Kalman filter on the convective scale. Quart. J. Roy. Meteor. Soc., 142(696), 1490-1504.
519	Borderies, M., Caumont, O., Delanoë, J., et al. 2019: Impact of airborne cloud radar reflectivity data
520	assimilation on kilometre-scale numerical weather prediction analyses and forecasts of heavy
521	precipitation events. Natural Hazards and Earth System Sciences, 19(4), 907-926.
522	Chen, F., Dudhia, J. 2001: Coupling an advanced land surface-hydrology model with the Penn State-
523	NCAR MM5 modeling system. Part I: Model implementation and sensitivity. Monthly Weather
524	Review, 129, 569-585.
525	Chen, H., Chen, Y., Gao, J., et al. 2020: A radar reflectivity data assimilation method based on
526	background-dependent hydrometeor retrieval: An observing system simulation experiment.
527	Atmospheric research, 243, 105022.
528	Chen, H., Gao, J., Wang, Y., et al. 2021: Radar reflectivity data assimilation method based on
529	background-dependent hydrometeor retrieval: Comparison with direct assimilation for real
530	cases. Quart. J. Roy. Meteor. Soc., 147(737), 2409-2428.
531	Chen, J., Xu, D., Shu, A., et al. 2023: The Impact of Radar Radial Velocity Data Assimilation Using
532	$WRF\text{-}3DVAR\ System\ with\ Different\ Background\ Error\ Length\ Scales\ on\ the\ Forecast\ of\ Super\ S$
533	Typhoon Lekima (2019). Remote Sensing, 15(10), p.2592.

- Courtier, P., Thépaut, J. N., Hollingsworth, A. 1994: A strategy for operational implementation of
- 4D-Var, using an incremental approach. Quart. J. Roy. Meteor. Soc., 120(519), 1367-1387.
- 536 Dowell, D. C., Wicker, L. J., Snyder, C. 2011: Ensemble Kalman filter assimilation of radar
- 537 observations of the 8 May 2003 Oklahoma City supercell: Influences of reflectivity
- observations on storm-scale analyses. Monthly Weather Review, 139(1), 272-294.
- 539 Dudhia, J. 1989: Numerical study of convection observed during the winter monsoon experiment
- using a mesoscale, two-dimensional model. Journal of the Atmospheric Sciences, 46, 3077-
- 541 3107.
- 542 Evensen, G. 1994: Sequential data assimilation with a nonlinear quasi-geostrophic model using
- Monte Carlo methods to forecast error statistics. Journal of Geophysical Research: Oceans,
- 544 99(C5), 10143-10162.
- 545 Gao, J., Xue, M., Brewster, K., et al. 2004. A three-dimensional variational data analysis method
- with recursive filter for Doppler radars. Journal of Atmospheric and oceanic technology, 21(3),
- 547 457-469.
- 548 Gao, J., Stensrud, D. J. 2012: Assimilation of reflectivity data in a convective-scale, cycled 3DVAR
- framework with hydrometeor classification. Journal of the Atmospheric Sciences, 69(3), 1054-
- 550 1065.
- 551 Gustafsson, N., Janjić, T., Schraff, C., et al. 2018: Survey of data assimilation methods for
- 552 convective-scale numerical weather prediction at operational centres. Quart. J. Roy. Meteor.
- 553 Soc., 144(713), 1218-1256.
- Hong, S. Y., Noh, Y., Dudhia, J. 2006: A new vertical diffusion package with an explicit treatment
- of entrainment processes. Monthly Weather Review, 134, 2318-2341.
- 556 Hu, M., Xue, M., Brewster, K. 2006: 3DVAR and cloud analysis with WSR-88D level-II data for
- 557 the prediction of the Fort Worth, Texas, tornadic thunderstorms. Part I: Cloud analysis and its
- impact. Monthly Weather Review, 134, 675-698.
- 559 Huang, L., Xu, D., Li, H., et al. 2023: Assimilating FY-3D MWHS2 Radiance Data to Predict
- 560 Typhoon Muifa Based on Different Initial Background Conditions and Fast Radiative Transfer
- 561 Models. Remote Sensing, 15(13), p.3220.
- Kain, J. S., Xue, M., Coniglio, M. C., et al. 2010: Assessing advances in the assimilation of radar

- data and other mesoscale observations within a collaborative forecasting-research environment.
- Weather and forecasting, 25(5), 1510-1521.
- Kong, R., Xue, M., Liu, C. 2018: Development of a hybrid En3DVar data assimilation system and
- 566 comparisons with 3DVar and EnKF for radar data assimilation with observing system
- simulation experiments. Monthly Weather Review, 146(1), 175-198.
- Kong, R., Xue, M., Liu, C., et al. 2020: Comparisons of hybrid En3DVar with 3DVar and EnKF for
- radar data assimilation: Tests with the 10 May 2010 Oklahoma tornado outbreak. Monthly
- 570 Weather Review, 149(1), 21-40.
- 571 Li, X., Ming, J., Wang, Y., et al. 2013: Assimilation of T-TREC-retrieved wind data with WRF
- 572 3DVAR for the short-term forecasting of typhoon Meranti (2010) near landfall. Journal of
- Geophysical Research: Atmospheres, 118(18), 10-361.
- 574 Li, X., Zeng, M., Wang, Y., et al. 2016: Evaluation of two momentum control variable schemes and
- 575 their impact on the variational assimilation of radar wind data: Case study of a squall line.
- Advances in Atmospheric Sciences, 33, 1143-1157.
- 577 Lindskog, M., Salonen, K., Järvinen, H., et al. 2004: Doppler radar wind data assimilation with
- 578 HIRLAM 3DVAR. Monthly weather review, 132(5), 1081-1092.
- 579 Lilly, D. K. 1990: Numerical prediction of thunderstorms-Has its time come? Quart. J. Roy. Meteor.
- 580 Soc., 116, 779-798.
- 581 Liu, C., Xue, M., Kong, R. 2019: Direct assimilation of radar reflectivity data using 3DVAR:
- Treatment of hydrometeor background errors and OSSE tests. Monthly Weather Review,
- 583 147(1), 17-29.
- Lopez, P. 2011: Direct 4D-Var assimilation of NCEP stage IV radar and gauge precipitation data at
- 585 ECMWF. Monthly Weather Review, 139(7), 2098-2116.
- 586 Mlawer, E., Taubman, S., Brown, P., et al. 1997: Radiative transfer for inhomogeneous atmospheres:
- 587 RRTM, a validated correlated-k model for the longwave. Journal of Geophysical Research,
- 588 102, 16663-16682.
- Navon, I. M. 2009: Data assimilation for numerical weather prediction: a review. Data assimilation
- for atmospheric, oceanic and hydrologic applications, 21-65.
- 591 Parrish, D. F., Derber, J. C. 1992: The National Meteorological Center's spectral statistical-

- interpolation analysis system. Monthly Weather Review, 120(8), 1747-1763.
- 593 Schenkman, A. D., Xue, M., Shapiro, A., et al. 2011: The analysis and prediction of the 8-9 May
- 594 2007 Oklahoma tornadic mesoscale convective system by assimilating WSR-88D and CASA
- radar data using 3DVAR. Monthly Weather Review, 139(1), 224-246.
- 596 Shen, F., Min, J., Xu, D. 2016: Assimilation of radar radial velocity data with the WRF Hybrid
- 597 ETKF--3DVAR system for the prediction of Hurricane Ike (2008). Atmospheric Research, 169,
- 598 127-138.
- 599 Shen, F., Xu, D., Min, J. 2019: Effect of momentum control variables on assimilating radar
- observations for the analysis and forecast for Typhoon Chanthu (2010). Atmospheric Research
- 601 234, 104771.
- 602 Shen F., Xu, D., Li, H., et al. 2020a: Impact of radar data assimilation on a squall line over the
- Yangtze-Huaihe River Basin with a radar reflectivity operator accounting for ice-phase
- hydrometeors. Meteorol Appl. 28, e1967.
- 605 Shen, F., Xu, D., Min, J., et al. 2020b: Assimilation of radar radial velocity data with the WRF
- hybrid 4DEnVar system for the prediction of hurricane Ike (2008). Atmospheric research, 234,
- 607 104771.
- 608 Shen, F., Min, J., Li, H., et al. 2021: Applications of radar data assimilation with hydrometeor control
- variables within the wrfda on the prediction of landfalling hurricane ike (2008). Atmosphere,
- 610 12(7), 853.
- 611 Shen, F., Song, L., Li, H., et al. 2022: Effects of different momentum control variables in radar data
- assimilation on the analysis and forecast of strong convective systems under the background
- of northeast cold vortex. Atmospheric Research, 280, 106415.
- 614 Simonin, D., Ballard, S. P., Li, Z. 2014: Doppler radar radial wind assimilation using an hourly
- 615 cycling 3D-Var with a 1.5 km resolution version of the Met Office Unified Model for
- 616 nowcasting. Quart. J. Roy. Meteor. Soc., 140(684), 2298-2314.
- 617 Sun, J., Crook, N.A. 1997: Dynamical and microphysical retrieval from Doppler radar observations
- using a cloud model and its adjoint. Part I: Model development and simulated data experiments.
- Journal of the Atmospheric Sciences, 54(12), 1642-1661.
- 620 Sun, J., Xue, M., Wilson, J. W., et al. 2014: Use of NWP for nowcasting convective precipitation:

- Recent progress and challenges. Bulletin of the American Meteorological Society, 95(3), 409-
- 622 426.
- 623 Tong, M., Xue, M. 2005: Ensemble Kalman filter assimilation of Doppler radar data with a
- 624 compressible nonhydrostatic model: OSS experiments. Monthly Weather Review, 133, 1789-
- 625 1807.
- Tong, C. C., Jung, Y., Xue, M., et al. 2020: Direct assimilation of radar data with ensemble Kalman
- filter and hybrid ensemble-variational method in the National Weather Service operational data
- assimilation system GSI for the stand-alone regional FV3 model at a convection-allowing
- resolution. Geophysical Research Letters, 47(19), e2020GL090179.
- Wan, S., Shen, F., Chen, J., et al. 2024: Evaluation of Two Momentum Control Variable Schemes in
- Radar Data Assimilation and Their Impact on the Analysis and Forecast of a Snowfall Case in
- 632 Central and Eastern China. Atmosphere, 15(3), 342.
- Wang, H., Sun, J., Fan, S., et al. 2013a: Indirect assimilation of radar reflectivity with WRF 3D-Var
- and its impact on prediction of four summertime convective events. Journal of Applied
- 635 Meteorology and Climatology, 52, 889-902.
- Wang, H., Sun, J., Zhang, X., et al. 2013b: Radar data assimilation with WRF 4D-Var. Part I: System
- development and preliminary testing. Monthly Weather Review, 141(7), 2224-2244.
- Kiao, Q., Kuo, Y. H., Sun, J., et al. 2005: Assimilation of Doppler radar observations with a regional
- 3DVAR system: Impact of Doppler velocities on forecasts of a heavy rainfall case. Journal of
- 640 Applied Meteorology, 44(6), 768-788.
- Kiao, Q., Kuo, Y. H., Sun, J., et al. 2007: An approach of radar reflectivity data assimilation and its
- assessment with the inland QPF of Typhoon Rusa (2002) at landfall. Journal of Applied
- Meteorology and Climatology, 46(1), 14-22.
- Xu, D., Shen, F., & Min, J. 2019: Effect of adding hydrometeor mixing ratios control variables on
- assimilating radar observations for the analysis and forecast of a typhoon. Atmosphere, 10(7),
- 646 415.
- Ku, D., Shu, A., Li, H., et al. 2021: Effects of Assimilating Clear-Sky FY-3D MWHS2 Radiance on
- the Numerical Simulation of Tropical Storm Ampil. Remote Sensing, 13(15), 2873.
- Ku, D., Yang, G., Wu, Z., et al. 2022: Evaluate radar data assimilation in two momentum control

650	variables and the effect on the forecast of southwest China vortex precipitation. Remote
651	Sensing, 14(14), 3460.
652	Zhao, K., Li, X., Xue, M., et al. 2012: Short-term forecasting through intermittent assimilation of
653	data from Taiwan and mainland China coastal radars for Typhoon Meranti (2010) at landfall
654	Journal of Geophysical Research: Atmospheres, 117(D6).